Effects of oxide additives on the hydrotalcite derived Ni catalysts for CO_2 reforming of methane

Juntian Niu[a,b], Shirley E. Liland[a], Jia Yang[a], Kumar R. Rout[c], Jingyu Ran[b*], De Chen[a*]

[a] Department of Chemical Engineering, Norwegian University of Science and Technology, Trondheim, 7491, Norway

[b] Key Laboratory of Low-grade Energy Utilization Technologies and Systems, Ministry of Education of PRC, Chongqing University, Chongqing, 400044, China

[c] SINTEF materials and chemistry, Trondheim, 7491, Norway

*Corresponding authors: De Chen and Jingyu Ran

E-mail: de.chen@ntnu.no; ranjy@cqu.edu.cn

Abstract: Here we provide new mechanistic and kinetic insights into the functions of oxides on Ni catalysts in methane dry reforming combining kinetic studies with density functional theory (DFT) calculations. Hydrotalcite derived Ni catalysts with a small amount of oxide additive (CeO_2, ZrO_2, ZnO) as promoters are synthesized and characterized by different techniques, X-ray diffraction (XRD), X-ray fluorescence (XRF), N_2 physisorption, H_2 chemisorption, transmission electron microscopy (TEM), scanning electron microscopy (SEM) and thermogravimetric analysis combined with mass spectrometry (TGA-MS). Regarding H_2/CO ratio, the CeO_2-Ni shows the highest the values along all the temperatures. Moreover, the CeO_2-Ni catalyst has the best stability among the four catalysts, while ZnO-Ni experiences the most severe deactivation. Kinetic studies in terms of reaction orders and activation energies are performed and compared to the DFT investigations, to assess the functions of oxide promoters. The CeO_2-Ni catalyst shows the lowest apparent activation energy for CO_2 activation, and it is also found that forward turnover rate is independent of CO_2 partial pressure for all the samples. In DFT calculations, CO_2 is more favorable to be activated on the support and the TOF obtained from G plot is in perfect agreement with our experiment value. In addition, it is also found that basicity and electron affinity of different oxide additives can be well correlated to the activation of CO_2 and catalyst deactivation. In general, both the increased basicity of oxide and electron affinity of metal help to promote the CO_2 activation and enhance the catalyst's stability. We propose that the CeO_2-Ni catalyst has best performance for CO_2 activation, thus leading to a higher surface oxygen concentration to oxidize the carbon on the catalysts, which prolongs the catalyst's life.

Keywords: Methane dry reforming; Oxide additive; Catalytic performance; Kinetic study; Basicity

1. Introduction

In recent decades, CO_2 utilization has become increasingly important because of escalating global warming phenomenon [1]. It is of great importance to reduce the emissions of greenhouse gases and also to further utilize processes capable of consuming these gases in both scientific research and industrial application [2,3]. Conversion of CO_2 to syngas via dry reforming of methane (DRM) has received considerable attention and prominent research interest [4,5]. Above all, this process provides a pathway to reduce and recycle greenhouse gases (CH_4 and CO_2) and convert them into syngas (H_2 and CO) [6]. In addition, the generation of syngas via methane is one of the most technically advanced routs for natural gas utilization [7]. On the other hand, the DRM reaction is seen as an attractive alternative for steam reforming of methane (SRM) because it can directly utilize raw natural gas and does not require subsequent gas separation and purification to remove CO_2 [8]. Furthermore, the produced syngas from DRM has a lower H_2/CO ratio than that from SRM, which is more suitable for further usage in the Fischer-Tropsch synthesis of long-chain hydrocarbons [9]. Moreover, dry reforming of methane is regarded as the basis for upgrading the calorific value of hydrocarbons for the solar reforming of natural gas process [10].

DRM is a highly endothermic reaction and requires a high operating temperature to attain high equilibrium conversion of CO_2 and CH_4 into H_2 and CO, and to minimize the thermodynamic driving force for coke formation [11]. Ni-based catalysts are considered as a promising candidate for this reaction owing to their low cost and high activity [12,13]. However, dry reforming of methane is inevitablely accompanied by catalysts deactivation due to carbon deposition through CO disproportionation ($2CO \rightarrow C + CO_2$) and methane decomposition ($CH_4 \rightarrow C + 2H_2$) [14,15]. The deactivation of catalyst due to coke formation is a major obstacle for the commercialization of methane dry reforming over the Ni catalysts. In addition, at high reaction temperatures, the sintering of Ni particles could also cause

catalyst deactivation [16–18]. Moreover, due to the occurrence of the reverse water gas shift reaction (rWGS: $H_2 + CO_2 \rightarrow CO + H_2O$), it would lead to the H_2/CO ratio lower than 1 [19,20]. Thus, single component Ni catalysts are not able to meet the stability and selectivity requirements [21]. There is an urgently need to develop a cost-effective, thermally stable and highly selective Ni catalyst without decreasing the initial activity.

In addition, during the DRM, CO_2 is activated and reduced into CO, it was reported that this process proceeds on the support instead of active metal alone [11,22,23]. Van Keulen et al. [24] found that the amount of adsorbed CO_2 molecules on ZrO_2 support was much greater than that of Pt atoms on the catalyst surface, suggesting that the ZrO_2 support, could adsorb and activate CO_2.

Ni-based catalysts with a small amount of oxide additive as promoter, have received increasing attention in recent years, both for their technological impact and scientific importance [25–28]. Oxide additive could improve Ni catalyst's resistance against deactivation, enhance H_2/CO ratio, and meanwhile, maintain their catalytic activity in DRM, thus providing an opportunity to design new catalysts with improved selectivity and stability without decreasing the initial activity. Koo et al. [25] reported that ceria promoted Ni/Al_2O_3 catalysts could markedly suppress the coke formation for combined steam and CO_2 reforming of methane through improving the Ni dispersion on the support. Similar results have been reported by Tsubaki [26]. They proved that joint promoter La_2O_3/CeO_2 could help to control the size of the Ni particle in methane dry reforming over Ni/Al_2O_3, thus improving coke resistance ability. In addition, Corthals et al. [27] used $MgAl_2O_4$ spinel powder as the support to prevent sintering of Ni for methane dry reforming. They observed that both CeO_2 and ZrO_2 promoted $Ni/MgAl_2O_4$ catalysts are promising for DRM. Moreover, CaO provides good performance for keeping catalysts from sintering [28], while with the Ca loading increasing, both the conversion of CH_4 and CO_2 decreased, which might be attributed to the increase in

Ni electron density.

Ni-containing hydrotalcite-derived catalysts have received increasing attention and been considered as promising catalysts for DRM [29–31]. It has been reported that after the calcination of such double-layered hydroxides, it results in a homogeneous mixture of well dispersed oxides having interesting physical-chemical properties and high thermal stability [32–35]. In addition, hydrotalcite-derived catalysts have basic properties resulting in higher strength of CO_2 adsorption, which is beneficial for the DRM reaction [30,31]. Experimental approaches have been exploited to gain deeper insight into the effect of oxide additives on Ni hydrotalcite-derived catalysts in DRM. Dębek et al. [36] found that incorporation of Ce into Ni-containing hydrotalcite-derived catalysts enhanced reducibility of nickel species, and meanwhile resulted in the formation of new strong basic sites, which improved catalytic stability in long-term reaction. Literature also reported that ceria has a high oxygen storage capacity (OSC) which is useful for the reaction in enhancing the reducibility within the fluorite lattice [37]. In addition, Dębek et al. [38] also investigated the Zr-promoted Ni hydrotalcite-derived catalysts in DRM. The presence of Zr could inhibit carbon nanofibers formation from CH_4 decomposition, and the ability of the Zr-containing catalysts to adsorb CO_2 on weak basic sites resulted in the formation of active carbonate species that were able to react with CH_4 through the DMR route. Although Zr promotion decreased activity, it strongly increased the stability and selectivity of the catalysts [39]. Moreover, ZrO_2 may increase the content of oxygen vacancies on the catalysts surface, which plays an important role for the dissociative adsorption of CO_2 [40,41]. In spite of well reported promotional effects of oxides in the methane dry reforming, a better fundamental understanding of the promotional effects is highly required.

Here we provide new mechanistic and kinetic insights into the functions of oxides on Ni catalysts in methane dry reforming combining reaction kinetics with DFT study. Hydrotalcite

derived Ni catalysts with a small amount of oxide additive (CeO_2, ZrO_2, ZnO) as promoters are synthesized and characterized by different techniques. Kinetic study in terms of reaction orders and activation energies are performed and compared to the DFT investigations, to assess the functions of oxide additives.

2. Experiment

2.1 Catalyst preparation

2.1.1 12wt% Ni catalyst

Monometallic 12wt% Ni derived from hydrotalcite-like precursor has been prepared by co-precipitation using metal nitrites component, the details is shown in Table S1 in the supporting information. An aqueous solution of NaOH and Na_2CO_3 (400 ml) was added at a constant rate into a reactor containing an aqueous mixtures of nitrates $Ni(NO_3)_2{\cdot}6H_2O$, $Mg(NO_3)_2{\cdot}6H_2O$ and $Al(NO_3)_3{\cdot}9H_2O$ (400 ml) in a period of 2 h [33–35]. After the addition was finished, the pH of mixture solution was adjusted to between 8 and 9. Then the reactor containing mixture solution was kept in the oil bath for 16 h at 80 ℃. The resultant hydrotalcite was cooled, then filtered and washed with deionized water several times. The hydrotalcite was then dried at 100 ℃ for 12 h (denoted as NiO-HT). And the prepared catalyst was confirmed to have typical hydrotalcite structures by XRD analysis. Subsequently, the catalyst was calcined in the air at 600 ℃ for 6 h, which destroyed the hydrotalcite structure and formed mixed oxides NiO/Mg(Al)O. The catalyst was crashed into powder and sieved to particle size between 75–125 μm.

Table 1 move to supporting information

Chemicals for 12 wt% Ni preparation.

	$Ni(NO_3)_2{\cdot}6H_2O$	$Mg(NO_3)_2{\cdot}6H2O$	$Al(NO_3)_3{\cdot}9H_2O$	NaOH	Na_2CO_3
Molar Ratio	0.37	2.63	1	8	0.5
Molar (mol)	0.02775	0.1972	0.0750	0.6000	0.0375
Mass (g)	8.070	50.575	28.135	24.000	5.962

2.1.2 Oxide additive (CeO_2, ZrO_2, ZnO) loading

In this paper, we prepared the promoted Ni-based catalysts through incipient wetness, impregnating the calcined hydrotalcite-derived Ni catalysts with additive precursor [$Ce(NO_3)_3 \cdot 6H_2O$, $ZrO(NO_3)_2 \cdot aq$ and $Zn(NO_3)_2 \cdot 6H_2O$]. The loading of promoter is fixed at about 3wt%. We checked the pore volume of Ni catalysts after calcination from N_2 physisorption. According to the pore volume, we determined the amount of the deionized water with calculated precursor salt used in the impregnation. The promoter catalysts firstly were dried at ambient temperature overnight, and then were re-calcined in air at 600 ℃ for 6 h, resulting in oxides. Finally, the catalysts were crashed into powder and sieved to particle size between 75–125 μm. The neat Ni catalyst, CeO_2, ZrO_2 and ZnO promoted Ni catalysts are named as Ni, CeO_2-Ni, ZrO_2-Ni and ZnO-Ni, respectively.

2.2 Catalyst characterization

XRD. XRD experiments were performed at ambient temperature on a Bruker D8 Advance DaVinci and diffractometer equipped with the Cu Kα radiation (λ = 1.54056 Å) X-ray source. XRD patterns were examined with 2θ values ranging from 20° to 80° at a scanning speed of 1°/min.

N_2 physisorption. Brunauer-Emmett-Teller (BET) surface area of the catalyst was measured by N_2 physical adsorption at liquid nitrogen temperature (Micromeritics, TriStar II 3020). All samples (100 mg) needed to be degassed under vacuum at 200 ℃ overnight prior to the test. The BET method was applied to calculate the specific surface area based on the N_2 isotherms. And the total pore volume was obtained at single point adsorption of pores less than 850.946 Å diameter at P/Po = 0.976709541 and the average pore size were acquired by BET model on the basis of the N_2 isotherms curve.

H_2 chemisorption. Metal dispersion was determined by hydrogen chemisorption performed at 40 ℃ (Micromeritics, ASAP 2020S). Calcined catalysts (100 mg) were loaded in tubular quartz reactor, evacuated at 40 ℃ for 1h and reduced in H_2 flow at 670 ℃ for 16 h.

After the reduction, the sample was evacuated for 0.5 h at 670℃ and subsequently for 1 h at 40 ℃. Then after the leak test pass, the sample was continuously evacuated for 0.5 at 40 ℃, at this temperature, an adsorption isotherm was recorded and the metal dispersion was determined based on the quantity of hydrogen uptake.

XRF. Metal oxides proportion was confirmed by XRF analysis (Rigaku, Supermini200). Calcined samples (100 mg) were mixed homogeneously with boric acid (around 2.5 g) and then pressed into pellets for test. The pellets were put into special sample holders and the test was completed in vacuum.

TGA-MS. Coke formation on spent catalysts was investigated by a TGA-MS (TGA: Netzsch STA 449C Jupiter, MS: Netzsch Aërlos QMS 403C) system under an air atmosphere. The experiments were conducted under an air stream (50ml/min), heating from ambient temperature to 1000 ℃, at a ramping rate of 10 ℃/min, and dwelling for half hour at this temperature. The amount of coke deposition was estimated by the mass loss in TGA analysis, confirming by MS results.

TEM. TEM images were taken and analyzed using a JEOL-2010F, with an accelerating voltage of 200 kV. The samples were prepared by ultrasonic dispersion of the reduced catalysts in ethanol. Drops of samples were put on a copper grid supported with a carbon film.

SEM. The morphology of spent catalysts were analyzed by SEM (FEI, APREO) to observe more details on coke formation and sintering of different samples, operated at 2.00 kV.

2.3 Catalytic test

Catalytic activity test was performed in a quartz fixed-bed tubular reactor (internal diameter: 10 mm) at atmospheric pressure. The catalyst bed consisted of 10 mg of the Ni or promoted Ni catalysts (75–125μm) diluted with inert 250 mg α-Al_2O_3 (75–125μm). Before testing, the catalysts were reduced at 670 ℃ for 16 h in a mixture of 1/1 H_2/Ar (total flow

100 mL/min). A series of mass flow controllers (Bronkhorst) allowed to feed reactant gas of 200 ml/min (CH_4:CO_2:Ar = 30:30:140, with a gas hourly space velocity (GHSV) of 1,200,000 $mL \cdot h^{-1} \cdot g_{cat}^{-1}$), and the GHSV is calculated from total flow. The Ar was used as balance and internal standard gas for CH_4 and CO_2 conversion calculations. A gas chromatograph (GC6890N, Agilent) using helium as the carrier gas was applied to analyze different gas species online including CH_4, CO_2, H_2, CO and Ar. The GC was equipped with a thermal conductivity detector (TCD), and water was removed prior to GC analysis. In activity test as well as selectivity test, the reaction temperature increased from 450 ℃ to 800 ℃ with an interval of 50 ℃, and the output data from GC was collected under steady-state for around 60 min at every temperature. In addition, stability test was performed at 700 ℃ for 30 h, CH_4:CO_2:Ar = 60:60:30 ml/min. And coke formation was investigated after 30 h stability test.

CH_4 and CO_2 conversions (X_{CH4} and X_{CO2}), H_2 and CO selectivity (S_{H2} and S_{CO}) as well as the H_2/CO ratio, were calculated as follows:

$$X_{CH4} = \frac{F_{CH4,in} - F_{CH4,out}}{F_{CH4,in}} \quad (1)$$

$$X_{CO2} = \frac{F_{CO2,in} - F_{CO2,out}}{F_{CO2,in}} \quad (2)$$

$$S_{H2} = \frac{F_{H2,out}}{2 \times (F_{CH4,in} - F_{CH4,out})} \quad (3)$$

$$S_{CO} = \frac{F_{CO,out}}{(F_{CH4,in} - F_{CH4,out}) + (F_{CO2,in} - F_{CO2,out})} \quad (4)$$

$$H_2 / CO = \frac{F_{H2,out}}{F_{CO,out}} \quad (5)$$

where $F_{i,in/out}$ is the molar flow rate of each species for feed gas (in) and effluent gas (out).

CH_4 and CO_2 average reaction rate (r_{CH4} and r_{CO2}) and average turnover frequency

(TOF_{CH4} and TOF_{CO2}) were calculated as follows at differential conditions:

$$r = \frac{X \cdot F}{W} = \frac{X \cdot F}{W \cdot 22414 \cdot 60} \cdot \frac{273.15}{298.15} (\text{mol} \cdot \text{s}^{-1} \cdot g_{cat}^{-1}) \quad (6)$$

$$TOF = \frac{r \cdot Mi}{fi \cdot D} = \frac{r \cdot M_{Ni}}{f_{Ni} \cdot D} (\text{s}^{-1}) \quad (7)$$

where X is the conversion, F is the gas flow rate, W is the catalysts weight, M_{Ni} is the molecular weight of Ni and f_{Ni} is the metal Ni weight fraction in catalysts. The dispersion D was estimated based on the Ni surface area of catalyst measured by hydrogen chemisorption.

For kinetic study, preliminary experiments were performed to eliminate external and internal mass and heat limitation. A high GHSV = 2,400,000 $mL \cdot h^{-1} \cdot g_{cat}^{-1}$ with a catalyst weight of 5 mg was applied to control all the methane conversion level less than 15% at a differential condition. The catalyst was diluted with inert 250 mg α-Al_2O_3 to minimize the temperature gradients and ensure the plug flow in the catalyst bed. The kinetic study was performed at temperatures from 450 ℃ to 550 ℃ with an interval of 25 ℃. The apparent activation energy for each sample from both CO_2 and CH_4 conversion were calculated according to the Arrhenius equation. In addition, CO_2 reaction order test was performed at the same GHSV applied in the activity test, at the temperature of 550 ℃, keeping the CH_4 partial pressure constant, adjusting the partial pressure of CO_2 and Ar.

2.4 DFT calculations

All the DFT calculations were conducted with a periodic slab model using the Vienna ab initio simulation program (VASP) [42,43]. Calculations were conducted with the generalized gradient approximation (GGA) and the BEEF-vdW exchange correlation functional [44]. Projector augmented wave (PAW) method was used to describe the electrons-ion interaction [45]. Five atomic layers Ni(111) surface were modeled, the bottom two layers were fixed at their equilibrium bulk positions, and the top three layers and the adsorbates were allowed to relax. And the plane wave cutoff energy of 400 eV was applied in the calculation of the

compact convergence. Additionally, a p(3 × 3) supercell was applied to neglect the surrounding adsorbate interactions in this work. DFT calculations considered spin-polarized electrons for Ni(111), due to the magnetic moment of Ni. A 15 Å vacuum region was used to ensure the intermolecular interaction between the slabs was negligible. In addition, a Fermi smearing of 0.2 eV was applied in present work. Brillouin zone integration was approximated by a sum over special k-points chosen using the Monkhorst–Pack method [46]. The meshes of 5 × 5 × 1 k-points for the Ni(111) surface. Moreover, transition states were searched through dimer method [47]. All the transition states were verified by frequency analysis, and only one imaginary frequency was identified for each transition state.

3. Results and discussion

3.1 Characterization of catalysts before reaction

3.1.1 XRD

X-ray diffraction patterns of the prepared hydrotalcite-like precursors and calcined samples with different oxide additive are shown in Fig. 1. Fresh hydrotalcite-like samples exhibit typical reflections at 2θ = 23.5°, 35°, 60.5° and 61.9°, corresponding to the (006), (009), (110) and (113) planes in the multilayer hydrotalcite structure [33,35]. No additional phases are observed, pointing to the successful incorporation of Ni into the hydrotalcite structure. The patterns acquired for the calcined samples show three main reflections at around 2θ = 36°, 43.5° and 63°, which could be assigned to the periclase-like structure of Ni-Mg-Al mixed oxides generated from the thermal decomposition of hydrotalcite samples [33,35]. The peak for CeO_2 [48], ZrO_2 [49,50] and ZnO [51] are weak, due to a small amount of oxide adding, the details are provided in Fig. 1.

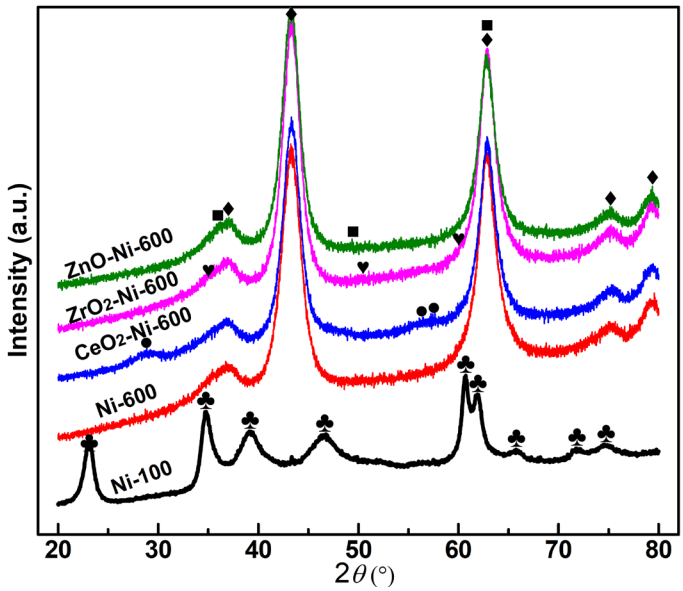

Fig. 1. XRD patterns of hydrotalcite-like precusors and calcined samples with different oxide additives. ♣ Hydrotalcite-like precusors; ♦ Mixed Oxide NiO-Mg(Al)O; ● CeO_2; ♥ ZrO_2 and ■ ZnO.

3.1.2 N_2 physisorption

Fig. 2 shows the nitrogen adsorption/desorption isotherms and pore size distribution of Ni catalysts with different oxide additives. The nitrogen adsorption/desorption isotherms of calcined samples can be categorized as type IV isotherms, typical of mesoporous materials [52,53]. The values of BET surface area for all samples range between 180 to 200 m^2/g_{cat}. And the total pore volume show a slight decrease with the adding of promoter, dropping from 0.42 to 0.35 cm^3/g. The similar trend is observed for average pore size, decreasing from 9.46 to 7.67 nm. Table 2 presents the BET surface area, pore volume and average pore diameter calculated from the N_2 adsorption/desorption isotherms.

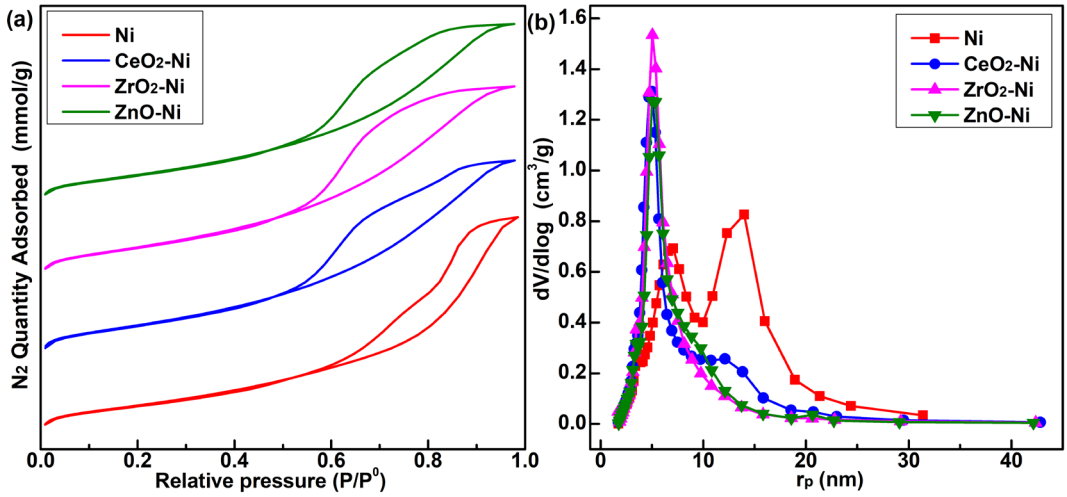

Fig. 2. Nitrogen adsorption/desorption isotherms and pore size distribution of Ni catalysts with different oxide additives.

Table 2

BET surface area, pore volume and average pore diameter calculated from N_2 adsorption/desorption isotherms.

Catalyst	BET Surface Area [m^2/g_{cat}]	Pore Volume [cm^3/g]	Average Pore Diameter [nm]
Ni	182.52	0.42	9.14
CeO_2-Ni	195.23	0.38	7.68
ZrO_2-Ni	198.27	0.38	7.68
ZnO-Ni	179.06	0.35	7.67

Ni loading ICP

3.1.3 H_2 chemisorption and TEM

The active surface area of Ni and promoted Ni catalysts was calculated from the quantity of hydrogen uptake, according to the assumption that the stoichiometry of H/Ni_s (surface nickel atom) is 1 [4,33]. Compared with pure Ni catalysts, the sample of Ni catalysts promoted by CeO_2 and ZrO_2 show a slight decrease in metallic surface area and total dispersion. In addition, similar trend is observed for ZnO promoted Ni catalys, the details are provided in Table 3.

Table 2

Metallic surface area and total dispersion of calcined samples.

Catalyst	Ni Loading [wt%]	Metallic Surface Area [m^2/g_{cat}]	Total Dispersion [%]
Ni	12.0	9.44	11.82
CeO_2-Ni	12.0	9.13	11.43
ZrO_2-Ni	12.0	9.33	11.68
ZnO-Ni	12.0	9.08	11.40

Fig. 3 shows the TEM images of Ni catalysts. Specifically, Fig 3a and 3b indicate that the average particle size of Ni catalysts is around 8.10 nm, the dispersion calculated by 1/d (d is the average particle size) is 12.34 %, which is in good agreement with the result from H_2 chemisorption (11.82 %). In addition, fringes of 0.20 nm of metallic Ni^0 was attributed to (111) planes [54] of Ni catalysts, as depicted in Fig. 3c.

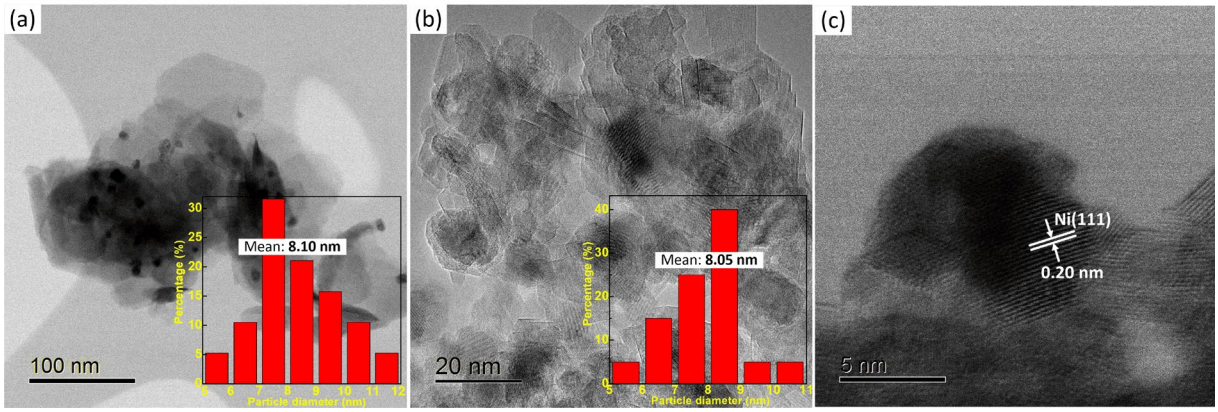

Fig. 3. TEM images of 12Ni catalysts (a) fresh sample, (b) reduced sample, and (c) surface lattice distance.

3.1.4 XRF

Table 4 provides the component of each sample after calcination. The XRF results showed that the loading of different oxide additives in Ni catalysts is 2.84 wt% for CeO_2, 2.76 wt% for ZrO_2 and 2.58 wt% for ZnO, respectively, which are all close to the nominal loading of 3.0 wt%, indicating that we have successfully synthesized the Ni catalysts with various oxide additives as promoter.

Table 4

Component of each sample after calcination.

Component (%)	Ni	CeO_2-Ni	ZrO_2-Ni	ZnO-Ni
MgO	58.30	56.07	59.03	56.47
Al_2O_3	24.21	22.48	24.17	22.89
NiO	16.81	15.5	12.99	14.94
Oxide additive		**2.84**	**2.76**	**2.58**

3.2 Activity and selectivity test

Fig. 4a and 4b shows the CH_4 and CO_2 conversion with the increase of temperature for Ni catalysts with different oxide additives. In order to see the intrinsic activity for different catalysts, we keep the conversion of reactants away from the equilibrium. The results indicates that the conversion of reactants increases with the temperature increasing. In addition, all of the promoted Ni catalysts presents slight lower activity compared with Ni catalyst. Specifically, at low temperature, the CeO_2-Ni, ZrO_2-Ni and ZnO-Ni have the similar conversion of CH_4 and CO_2, while at high temperature, the activity follows the trend: CeO_2-Ni > ZrO_2-Ni > ZnO-Ni. Moreover, due to the occurrence of reverse water gas shift reaction, the conversion of CO_2 is higher than that of CH_4 [55,56].

Fig. 4c and 4d provides the H_2 selectivity and CO selectivity, respectively. The CeO_2-Ni has the best performance for H_2 selectivity, it is higher than the other three in the whole process, and reaches 1 at 650 ℃. Regarding the CO selectivity, ZrO_2-Ni stands out among four samples, it is up to 1 at 550 ℃, while for ZnO-Ni, it neither enhances the H_2 selectivity nor the CO selectivity, even it is worse than the Ni catalyst. Furthermore, Fig. 4e depicts the H_2/CO ratio with the increase of temperature for different samples. The CeO_2-Ni shows the highest value along all the temperatures, and also firstly reaches 1 at 650 ℃, which indicates that it could suppress the rWGS reaction, thus CeO_2-Ni is considered as a promising candidate for this reaction in terms of selectivity.

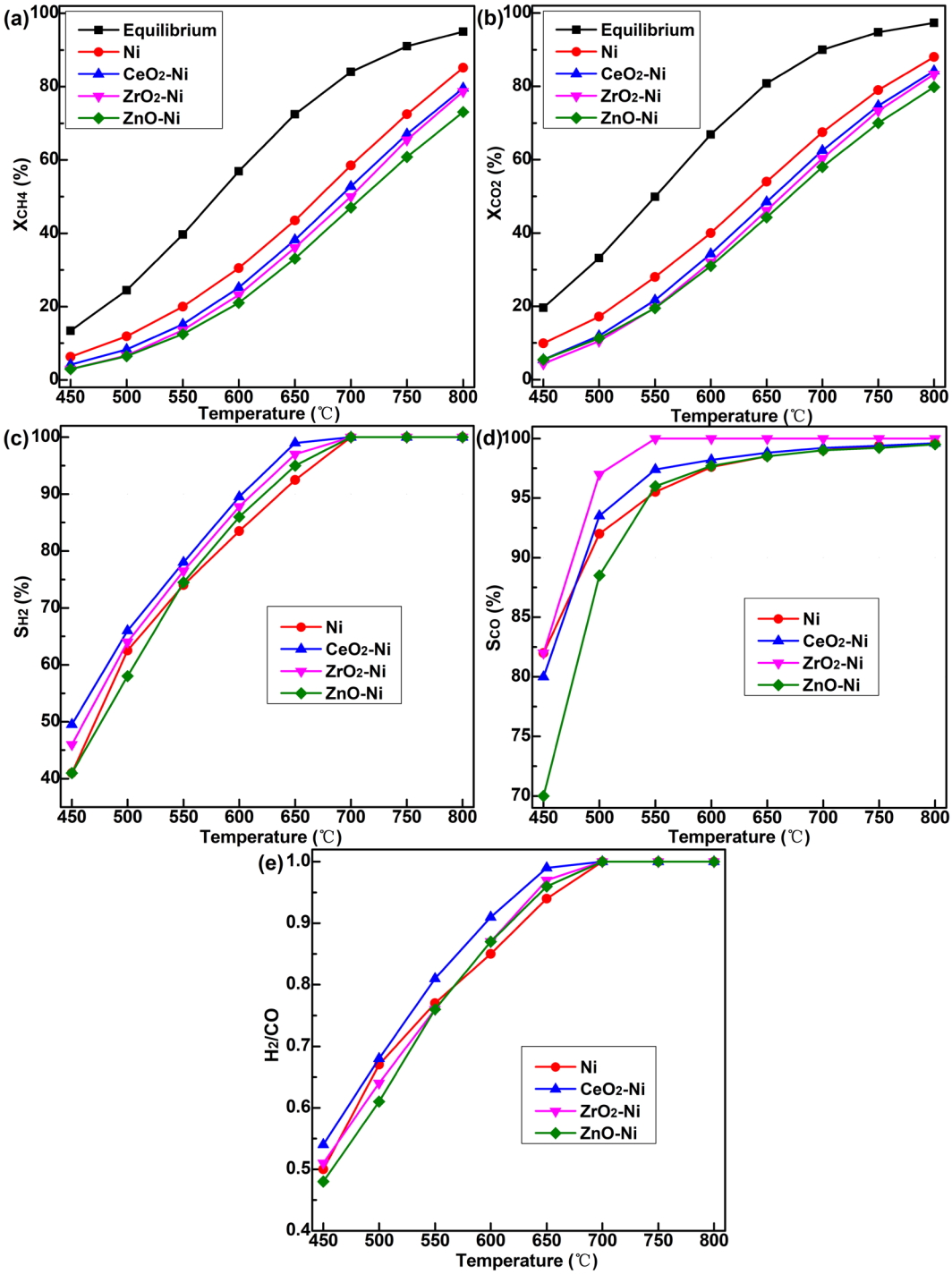

Fig. 4. Activity and selectivity test of catalysts for DRM: (a) CH_4 conversion; (b) CO_2 conversion; (c) H_2 selectivity; (d) CO selectivity and (e) H_2/CO ratio. Reaction conditions: $CO_2/CH_4/Ar$ = 30/30/140 mL/min, GHSV = 1,200,000 $mL \cdot h^{-1} \cdot g_{cat}^{-1}$, 1 atm.

3.3 Rate and TOF remove??

In order to compare activity for different samples, we have calculated the average reaction rate and TOF from both CH_4 and CO_2 sides at all temperatures. Table 5 and 6 give

the average reaction rate of CH_4 and CO_2, respectively. It is found that average reaction rate increases with the temperature increasing. Generally, the average reaction rate follows the order: Ni > CeO_2-Ni > ZrO_2-Ni > ZnO-Ni. Additionally, the average reaction rate of CO_2 is slightly higher than the CH_4 average reaction rate, due to the occurrence of rWGS reaction. In addition, Fig. 5 presents the TOF for different samples with the increasing temperature, similar trend is observed with average reaction rate. There is a slight decrease in activity (TOF) for CeO_2-Ni and ZrO_2-Ni, compared with Ni.

Table 5

CH_4 average reaction rate at different temperatures. Reaction conditions: $CO_2/CH_4/Ar$ = 30/30/140 mL/min, GHSV = 1,200,000 $mL \cdot h^{-1} \cdot g_{cat}^{-1}$, 1 atm.

Temperature (°C)	CH_4 average reaction rate ($mmol \cdot s^{-1} \cdot g_{cat}^{-1}$)			
	Ni	CeO_2-Ni	ZrO_2-Ni	ZnO-Ni
450	0.129	0.086	0.061	0.061
500	0.243	0.170	0.137	0.133
550	0.409	0.311	0.278	0.255
600	0.623	0.517	0.476	0.437
650	0.889	0.783	0.738	0.676
700	1.200	1.079	1.032	0.960
750	1.482	1.371	1.339	1.243
800	1.741	1.627	1.608	1.494

Table 6

CO_2 average reaction rate at different temperatures. Reaction conditions: $CO_2/CH_4/Ar$ = 30/30/140 mL/min, GHSV = 1,200,000 $mL \cdot h^{-1} \cdot g_{cat}^{-1}$, 1 atm.

Temperature (°C)	CO_2 average reaction rate ($mmol \cdot s^{-1} \cdot g_{cat}^{-1}$)			
	Ni	CeO_2-Ni	ZrO_2-Ni	ZnO-Ni
450	0.194	0.112	0.090	0.112
500	0.351	0.243	0.215	0.231
550	0.572	0.441	0.403	0.399
600	0.817	0.701	0.656	0.634
650	1.104	0.993	0.944	0.903
700	1.379	1.277	1.236	1.185
750	1.615	1.529	1.498	1.432
800	1.800	1.721	1.702	1.631

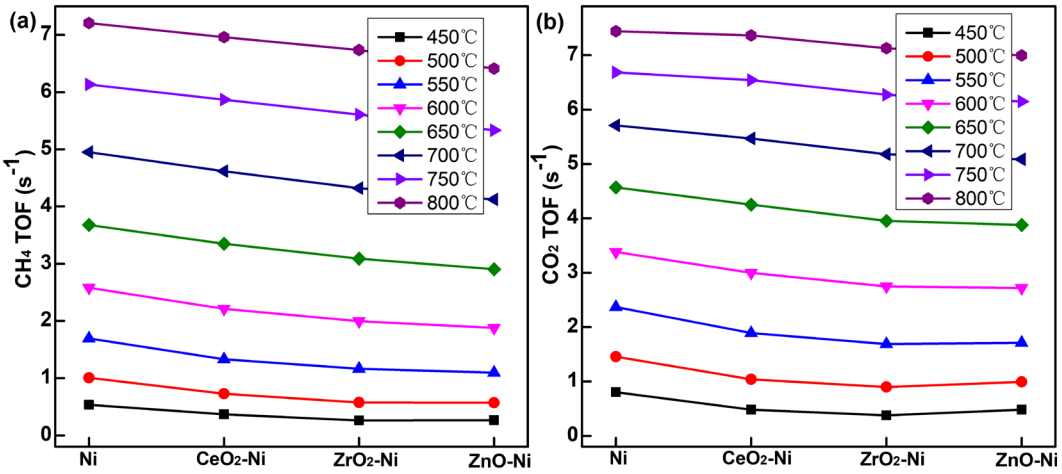

Fig. 5. TOF for different samples with the increasing temperature from (a) CH_4 and (b) CO_2 conversion.

Reaction conditions: $CO_2/CH_4/Ar$ = 30/30/140 mL/min, GHSV = 1,200,000 $mL \cdot h^{-1} \cdot g_{cat}^{-1}$, 1 atm.

3.4 Stability test

Stability tests are performed at 700℃ after 30 h running. As seen from Fig. 6a, the Ni and ZnO-Ni present a larger decrease of CO_2 conversion compared with the sample of CeO_2-Ni and ZrO_2-Ni. To clearly show the degree of deactivation for all samples, we normalize it by dividing the initial conversion for each catalyst, as shown in Fig. 6b. Compared with the Ni catalyst, the ZrO_2-Ni catalyst shows a similar deactivation behavior, and the stability is slightly better than Ni sample. In addition, CeO_2-Ni has the best stability among the four samples, while ZnO-Ni experiences the most severe deactivation. As a consequence, the stability follows the order: CeO_2-Ni > ZrO_2-Ni > Ni > ZnO-Ni. Moreover, we define the deactivation factor as follows:

$$\alpha = 1 - X(20) / X(0) \tag{8}$$

where α is the deactivation factor, X(20) and X(0) represent the conversion of CO_2 after 20 h and initial value, respectively.

The deactivation factor α is according to the following sequence: 0.06 [CeO_2-Ni] < 0.09 [ZrO_2-Ni] < 0.10 [Ni] < 0.15 [ZnO-Ni], the bigger value of α, the worse the stability is.

Therefore, we conclude that the stability of Ni catalyst can be significantly improved by adding CeO_2.

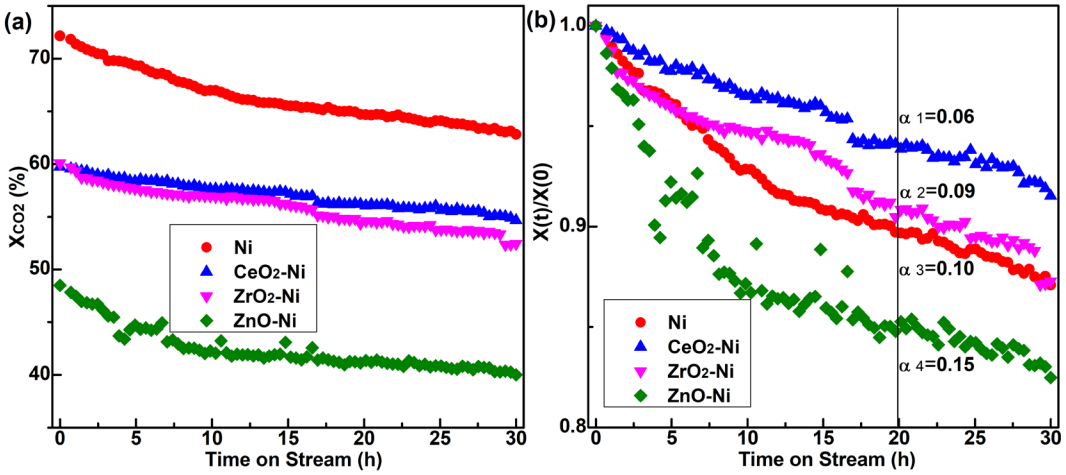

Fig. 6. Stability test of catalysts for DRM: (a) X_{CO2}; (b) X(t)/X(0). Reaction conditions: $CO_2/CH_4/Ar$ = 60/60/30 mL/min, 700 °C, 1 atm, 30 h.

3.5 Role of oxide additive in the stability of the catalysts

Coke formation and sintering are the two dominant reasons for causing the catalysts deactivation. In the following sections, we present the TGA plot of spent samples after stability test to check the amount of coke formation, as well as generated CO_2 signal by MS. In addition, for the morphology of spent catalysts have been inspected by SEM, providing more information on coke formation and sintering.

3.5.1 TGA–MS analysis

The temperature programmed oxidation (TPO) was conducted under an air stream (50ml/min), heating from ambient temperature to 1000 °C, at a ramping rate of 10 °C/min, and dwelling for half hour at this temperature. The amount of coke deposition was estimated by the mass loss in TGA analysis, confirming by MS results, as seen from Fig. 7. Generally, the mass loss curves can be divided into three major ranges. From ambient temperature to 220 °C, the mass loss mainly due to the moisture removal. The second range is from 220 °C to 350 °C, the oxidation of reduced Ni causes a small increase in weight. The most important range is from 350 °C to 800 °C, the deposited carbon oxidation and elimination leads to the

mass loss, which could be confirmed by CO_2 signal from MS. It is demonstrated that adding a small amount of oxide additive into Ni catalysts could markedly suppress the carbon formation. In addition, CO_2 peaks (Fig. 7b) of TPO of carbon formed on oxide promoted Ni catalysts shifted to lower temperatures compared to the Ni catalyst, indicating that the carbon deposited on the oxide promoted catalysts is softer and less crystallized than one on Ni catalyst.

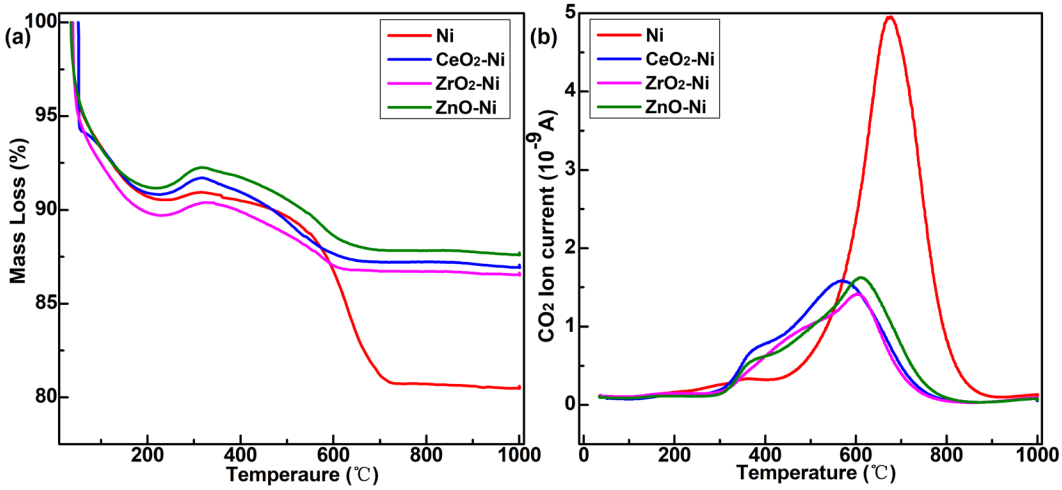

Fig. 7. (a) TGA analysis after stability test; (b) CO_2 signal from MS.

3.5.2 SEM analysis

SEM images of spent catalysts with different oxide additives after 30 h running are shown in Fig. 8. As seen from the figures, significant amount of filamentous carbon was observed over the spent Ni, while the promoted Ni with oxide additives showed much less filamentous carbon formation. Especially for ZrO_2-Ni and ZnO-Ni, the filamentous carbon was hardly observed on these samples. Literature [52] reported that carbon whisker almost does not paly the dominate role in causing the deactivation, therefore, although a small amount of filamentous carbon was formed on the CeO_2-Ni catalysts, it can still keep the best stability among four catalysts. In addition, according to the stability test, the ZnO-Ni experienced the most severe deactivation. However, very little filamentous carbon was observed on this sample after stability test, combined with the TGA-MS analysis, carbon

oxidation leads to the mass loss, so we infer that the encapsulated carbon dominates the coke deposition on this catalyst, which could block the active sites of metal surface and bring about the deactivation of catalysts [14].

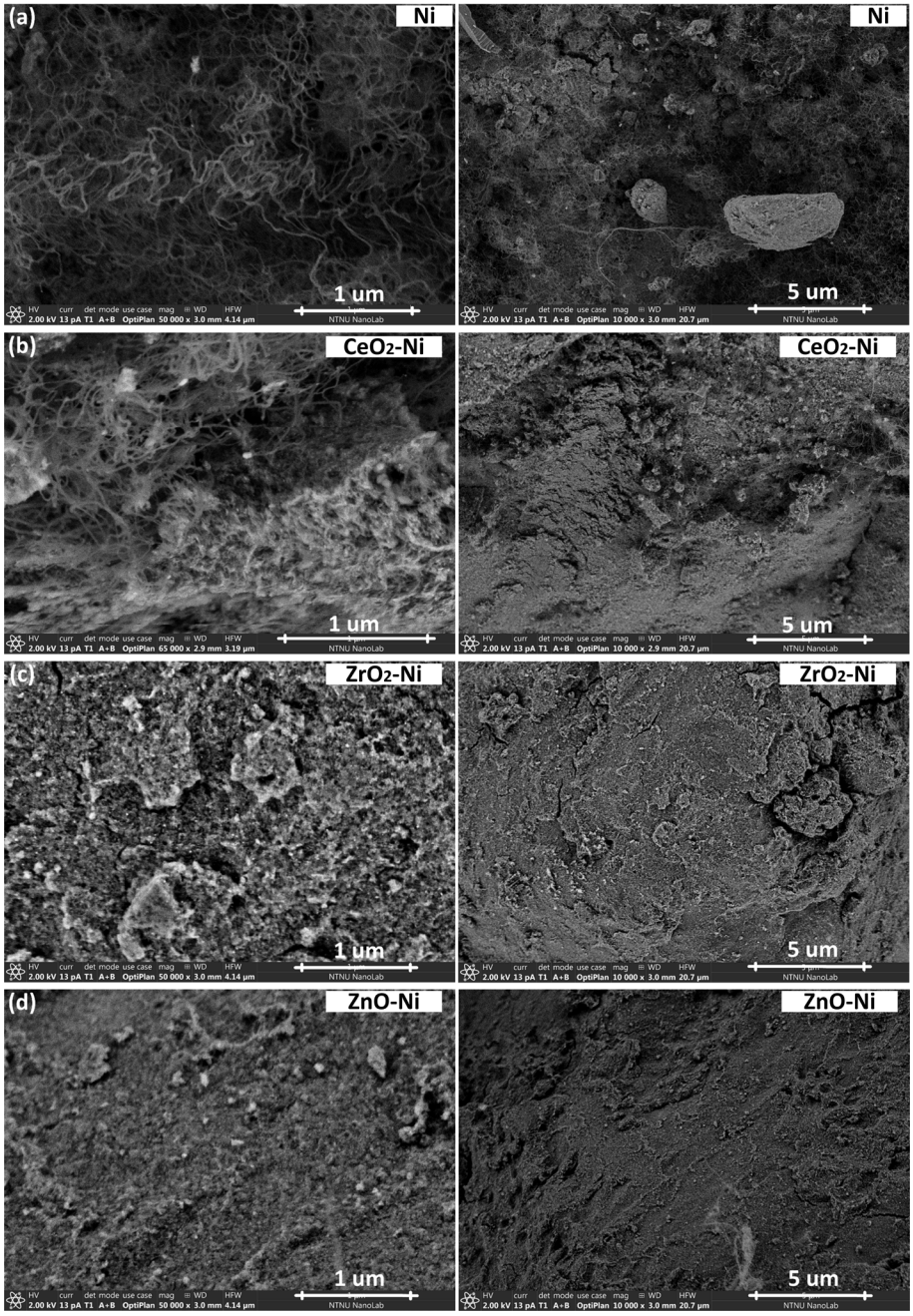

Fig. 8. SEM images after stability test: (a) Ni; (b) CeO_2-Ni; (c) ZrO_2-Ni; and (d) ZnO-Ni.

3.6 Kinetic study

3.6.1 Apparent activation energy

In order to control the reaction at the differential condition, the experiments of kinetic

study was performed at the methane flow based GHSV of 720,000 mL•h-1•gcat-1 from 450 ℃ to 550 ℃ with an interval of 25 ℃. The reaction rates of CH_4 and CO_2 based on the catalyst and Ni weight are presented in Table S2 and S3, respectively in the supporting information. Fig. 9 displays the Arrhenius plot for TOF of CH_4 and CO_2 on each catalyst with 25 K temperature increment, from 723 to 823 K. Generally, the apparent activation energy for CH_4 conversion of promoted samples are all higher than that on Ni catalyst. The values of activation energy on CeO_2-Ni and ZnO-Ni are 78.69 kJ/mol and 78.21 kJ/mol, respectively, higher than that of 70.69 kJ/mol on ZrO_2-Ni. In addition, regarding the CO_2 conversion, both CeO_2-Ni and ZrO_2-Ni show a little bit lower activation energy compared with Ni, while ZnO presents a higher activation barrier. It is suggested that the oxide additive CeO_2-Ni and ZrO_2-Ni could lower the energy for CO_2 activation, thus promoting the CO_2 dissociation into CO and O. Furthermore, the produced O species play the key role for CH_x and surface carbon oxidation, which affects the H_2/CO ratio and the formed surface carbon amount.

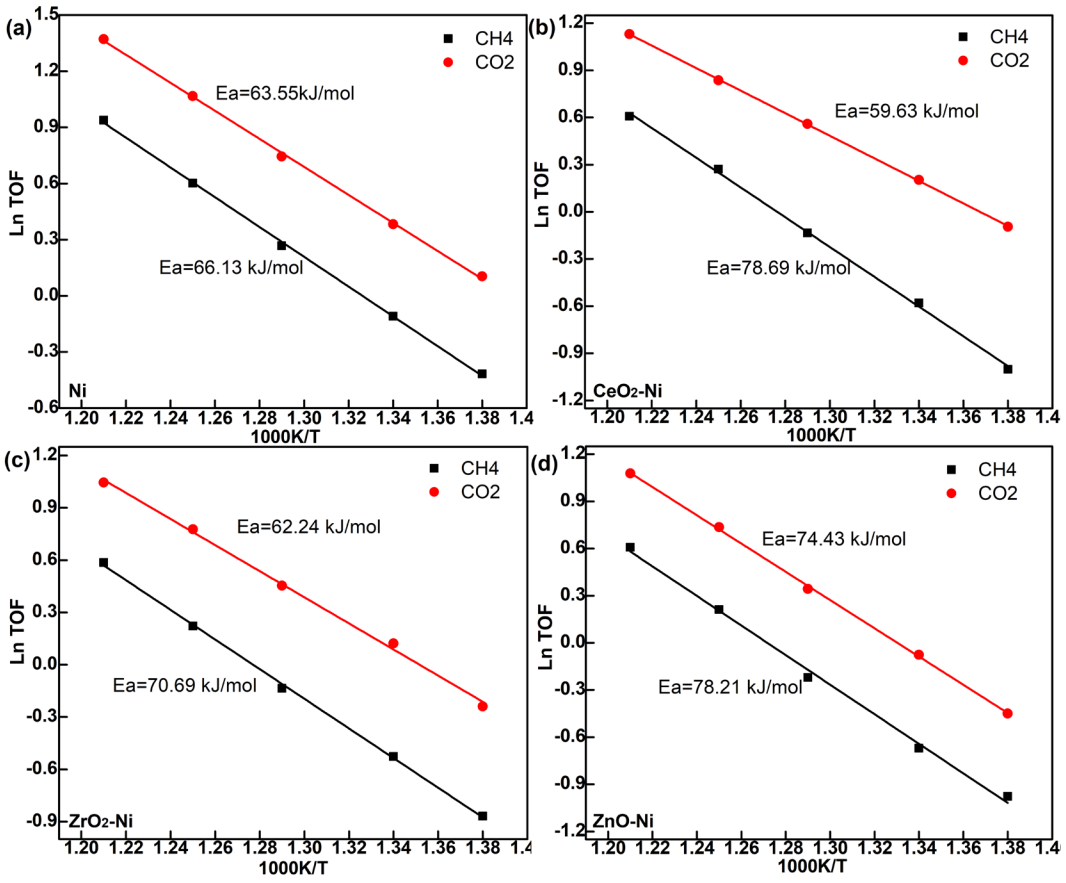

Fig. 9. Arrhenius plot for TOF of CH_4 and CO_2 on each catalyst with 25 K temperature increment: (a) Ni; (b) CeO_2-Ni; (c) ZrO_2-Ni; and (d) ZnO-Ni. Reaction conditions: $CO_2/CH_4/Ar$ = 30/30/140 mL/min, GHSV = 2,400,000 $mL \cdot h^{-1} \cdot g_{cat}^{-1}$, 1 atm.

3.6.2 CO_2 Reaction order

Effect of CO_2 partial pressure on forward TOF of CH_4 has been shown in Fig. 10. It can be clearly seen that CH_4 forward turnover rate is not influenced by CO_2 partial pressure, which has been reported in Wei and Iglesia study [57], the CO_2 reaction order is approaching to 0. However, CO_2 reaction order of 1 was found by in Özkara-Aydınoglu and Aksoylu [58]. It is worth noting that the support is MgO of Wei and Iglesia study, while later one is Al_2O_3. In this paper, the ratio of Mg:Al is approximately close to 2.63:1, so MgO dominates the main properties of the support. The generated Mg(Al)O mixed oxides from calcination of hydrotalcite is basic [31,32]. Thus, CO_2 reaction order found in this paper is similar to the one in Wei and Iglesia's study.

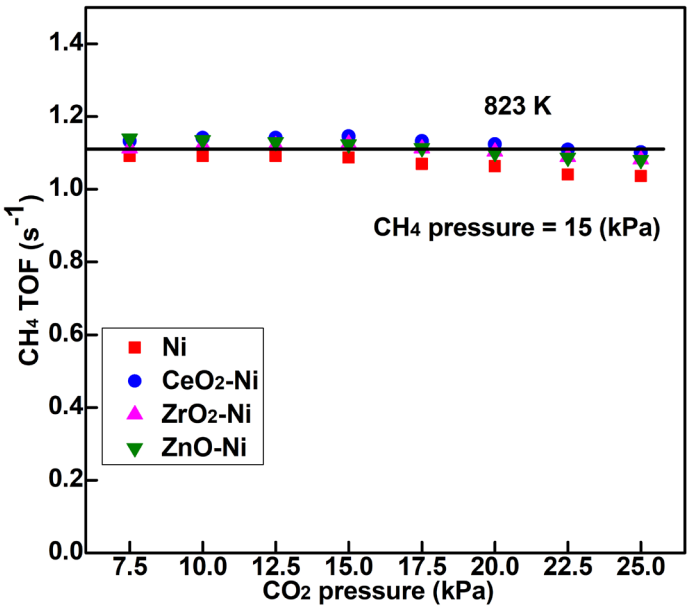

Fig. 10. Effect of CO_2 partial pressure on forward TOF of CH_4 (balance Ar, total pressure = 100 kPa).

Zero order of CO_2 reaction suggests that the CH_x (1-4) dissociation is the rate-determining step (RDS), in good agreement with Wei and Iglesia's [57] work. Obviously, the reaction mechanism and kinetics could depend on the support properties, which will be

discussed in a more detail in the next section.

3.7 DFT calculations for CH_4/CO_2 reforming reaction on Ni

DFT calculation of adsorption of intermediates and free energy of reaction pathway of CH_4/CO_2 reforming is performed to gain a better kinetic insight of effects of catalyst properties. The elementary steps involved in the mechanism is presented in Fig. 11. All the thermodynamic properties were calculated at a temperature of 1023 K. The standard molar Gibbs free energy for each species in methane dry reforming follows [12]:

$$G^0 = E_{\text{total}} + E_{ZPE} + \gamma RT(1+In\frac{P}{P^0}) + U^0 - TS^0 \quad (9)$$

where E_{total} is the total energy obtained from DFT calculations, and E_{ZPE}, U^0 and S^0 are the correction energy from zero-point energy (ZPE), thermal energy and entropy, respectively. R is the gas constant, P is the partial pressure of the gas-phase molecule, γ is 0 for the surface adsorbed species and 1 for gaseous molecule.

We plot the Gibbs free energy for methane dry reforming on Ni catalyst, both CO_2 activation on the metal surface and support have been considered, as depicted in Fig. 11. Although it might be a small free energy for activation of CO_2 on support and surface diffusion to metal, here we simplify and treat it as an extreme case of zero entropy change of CO_2 activation on Ni surface.

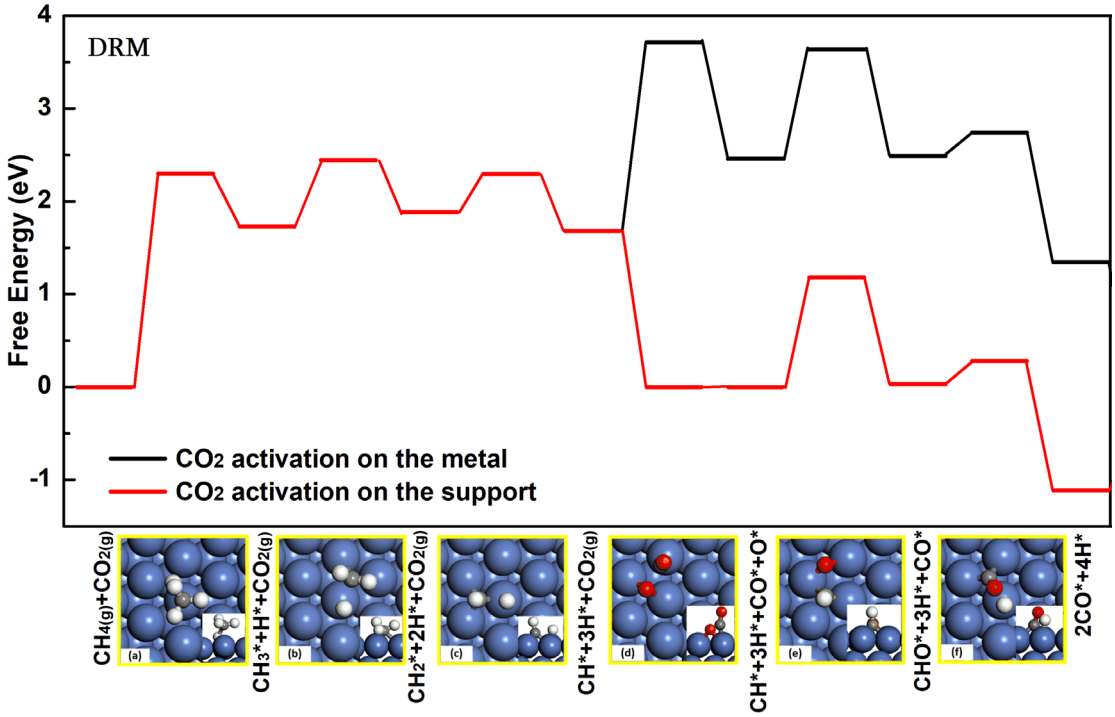

Fig. 11 Free energy landscape in DRM on Ni surface: CO_2 activation on the metal surface (in black) and on the support (in red). Reaction conditions: P_{CH4} = 0.15 bar, P_{CO2} = 0.15 bar, P_{Ar} = 0.70 bar, T = 1023 K. Transition states on Ni surface: (a) CH_4--CH_3+H; (b) CH_3--CH_2+H; (c) CH_2--CH+H; (d) CO_2--CO+O; (e) CH+O--CHO; and (f) CHO--CO+H.

It can be clearly seen from Fig. 11 that the rate-determining step depends significantly on the CO_2 activation mechanism due to the large ΔG of the CO_2 activation step on the Ni surface. When the CO_2 activates at the Ni surface, CO_2 activation and CH*+O* step have similar free energy with the highest free energy in the ΔG profile. These two steps are kinetic relevant steps for DRM which is contradict with the experimental observation CH_x (1-4) that dissociation is the rate-determining step. When CO_2 activates on the oxides lowered significantly the total energy, the CH_x (x = 2-4) dissociation steps have similar free energy with the highest free energy in the ΔG profile. The CH_x (x = 2-4) dissociation steps are kinetic relevant steps, in good agreement with the experimental observation. The turn over frequency (TOF) could also be calculated as follows based on the highest point of G plot:

$$TOF_{DFT} = \frac{k_b T}{h} \exp(\frac{-\Delta G}{RT}) P_{CH4} P_{H2}^{n} \quad (10)$$

where k_b is the Boltzmann constant, T is the reaction temperature, h is the Planck constant, ΔG is the highest point of G plot, R is the gas constant, P_{CH4} is the partial pressure of CH_4, and P_{H2} is the partial pressure of H_2, due to the second C–H bond activation is regarded as the *RDS*, here reaction order for H_2 n = - 0.5.

The highest Gibbs free energy is around 240 kJ/mol, TOF_{DFT} is 5.92 s^{-1} at 1023 K accordingly, which is very close to our experiment value TOF_{EXP} 6.13 s^{-1} at 1023 K. For the CO_2 activation on Ni surface, the highest Gibbs free energy is around 360 kJ/mol, which corresponds to a TOF of 4.42×10^{-6} s^{-1}, far lower than the experimental one. Therefore, based on both the kinetic and DFT results, it can be concluded that CO_2 activation on oxides plays a significant role in DRM reaction.

3.8 Functions of oxide additive

CO_2 is a mildly acidic molecule and it is normally attracted by the basic sites of solid surfaces. However, the nature of the CO_2 molecule is regarded amphoteric due to the electron-deficient C atom and the electron-rich O atom. The activation of CO_2 on the solid surface depends on its basicity. Generally metal oxides are acid-base materials which can be categorized into basic (e.g. MgO), acidic (e.g. γ-Al_2O_3), amphoteric (e.g. CeO_2, $ZrO_2$and ZnO) and neutral (SiO_2) materials. The metal cations (M^{n+}) interact with the electron-rich O atom in CO_2 as Lewis acid, while the O^{2-} chemically interacts with the electron deficient basic C atom in CO_2 molecule as Lewis base. CO_2 activates over surface M^{n+}-O^{2-} pairs on the boundaries of metals and supports or supports, followed by its subsequent dissociation into CO and O, as well as surface diffusion. Electronegativity is the tendency to attract electrons, or to stabilize negative charges. An oxygen bound to a less-electronegative metal atom will be a stronger base (add refs). We plotted Ea_{CO2} and deactivation factor as a function of electronegativity of cations in the oxides [64], as a descriptor in Fig. 12. In general, both Ea_{CO2} and α decrease with decreasing electronegativity of cations in the oxides. As shown in

Figure 12, the basicity of oxide additives increases in an order: CeO_2 > ZrO_2 > ZnO [60–63], (refs) with decreasing electronegativity of cations, in a good agreement of with the literature. Ce in CeO_2 with the lower electronegativity and O^{2-} with strong Lewis basicity interact more strongly with CO_2 molecule which destabilize the transition state structure thus enhance the activation via dissociation of CO^2* to CO* and O*, and lower the activation energy of CO_2 activation.

The Ni surface areas of promoted catalysts is only slightly lower than the neat Ni catalyst (Table 2). In addition, no obvious peaks corresponding to the oxide additives in the XRD patents were observed. These results suggest that the oxides are most likely well dispersed on the support. However, it is difficult to estimate the dispersion of oxide additives. Anyhow, a well dispersed oxides with high activity of CO_2 adsorption and dissociation, located nearby the metal particles and a fast surface diffusion are highly desired. It has been reported that the metal and oxide interface is the active sites for CO_2 dissociation (ACS Catal. 2016, 6, 4501−4505). The insights provided here could rationalize the literature observations. Van Keulen et al. [24] also observed that conversion of CO_2 was greater for Pt/ZrO_2 compared to Pt/Al_2O_3 at the same Pt loading. This varying activity towards CO_2 activation could be attributed to the greater basicity of the ZrO_2 support and the presence of O deficiencies. In contrast, Mark et al. [59] found that Al_2O_3, which is acidic in nature, does not help to activate the mildly acidic CO_2.

The fact that the apparent activation energy of CO_2 activation depends on the electronegativity of cations in the oxide additives suggests the activation on the added oxides is domination for CO_2 activation while the surface diffusion is relatively fast and not kinetically relevant. Figure 12b clearly illustrates the deactivation function is a function of electronegativity of cations of the oxides. The lower deactivation function, indicating a lower deactivation rate and better catalyst stability, was obtained at a lower electronegativity. The

enhanced CO_2 activation at lower electronegativity promoted generation of O*. Through diffusion of O* into Ni surfaces, it enhanced the surface reaction steps of CHx with O* and thus reduced the coke formation and stabilized the catalysts.

In addition, it should be noted that the Al-Mg mixed oxide obtained from calcination of hydrotalcite like materials is also basic. The exact electronegativity of the support without oxide promotion is unknown. We try to apply the relationship in Fig. 12a to unknown catalysts. Based on the activation energy of CO_2, the electronegativity for Ni catalyst without promoter can be predicted to be approximately ?? kJ/mol. Plotting the predicted electron affinity and experimental deactivation factor in Fig. 12b, it fits well the tendency of the deactivation factor as a function of electron affinity. It proves an applicability of these two plots in catalyst design. Both the increased basicity of oxide and electron affinity of metal help to promote the CO_2 activation and enhance the catalyst's stability. We propose that CeO_2-Ni has best performance for CO_2 activation, thus leading to a higher concentration of surface oxygen to oxidize the carbon on the catalysts, which prolongs the catalyst's life.

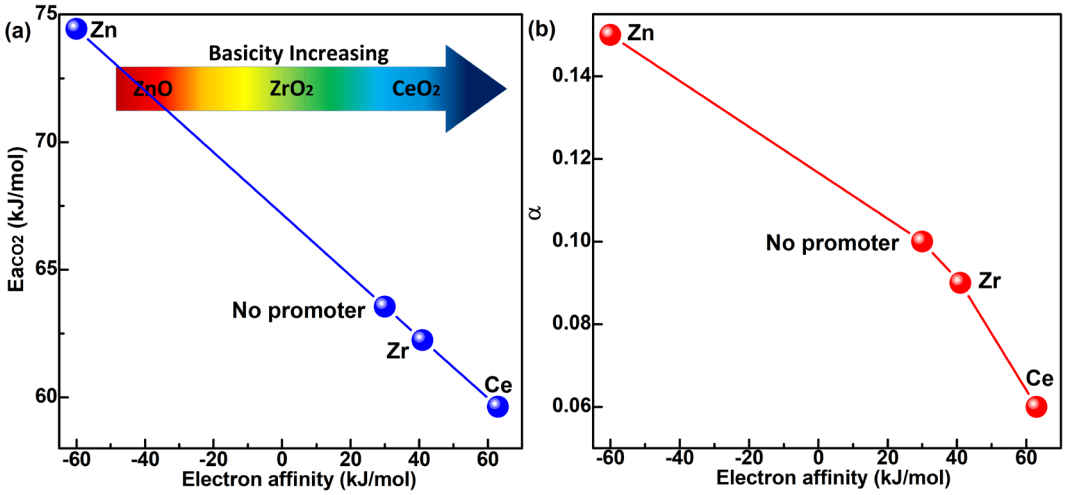

Fig. 12. (a) Ea_{CO2} and (b) deactivation factor as a function of electron affinity of metal in the oxides.

The plot in Fig. 12 provides a principle for catalyst design for DRM to achieve better stability. Oxides consisting of cations with lower electronegativity such as Bi (91), Sb (101),

Sn (107) etc [64] are predicted to be good candidates for promoters of Ni catalysts, which will be investigated in future.

4. Conclusions

Through impregnating oxide additives (CeO_2, ZrO_2 and ZnO) into the 12 wt% Ni hydrotalcite-derived catalysts, we synthesized thermally stable and highly selective promoted Ni catalyst for methane dry reforming reaction. All the promoted Ni catalysts presented slightly lower activity compared to the Ni catalyst. CeO_2-Ni catalyst exhibited the highest H_2/CO ratio along all the temperatures and the best stability. DFT calculation assisted kinetic analysis and experimental kinetic study reveal the dependence of the rate-determining step on the CO_2 activation. For the fast oxide assisted CO_2 activation process, the methane activation became the rate-determining step. Promotion of Ni catalyst by oxides such as CeO2, ZrO2 and ZnO enhanced CO_2 activation. The activation energy decreased and stability increased with decreasing electronegativity of cations of oxide additives and CeO_2-Ni catalyst has the lowest apparent activation energy for CO_2 activation and the best stability. The enhanced CO_2 activation increased the surface oxygen concentration, which promoted oxidation of the surface carbon species, thus reduced carbon formation and improved the catalyst stability. This work presents new mechanistic and kinetic insights into the functions of oxides on Ni catalysts in methane dry reforming combing kinetic studies and DFT calculations, identified electronegativity of the cations of the oxide additive as a descriptor, which could provide principles for catalysts design to improve stability and selectivity of Ni based catalysts.

Acknowledgment

The authors would like to thank the Project Supported by Graduate Scientific Research

and Innovation Foundation of Chongqing, China (Grant No. CYB16022), China Scholarship Council (Grant No. 201606050054), and Department of Chemical Engineering, Norwegian University of Science and Technology, Norway.

References

[1] Y. Kathiraser, U. Oemar, E.T. Saw, Z. Li, S. Kawi, Kinetic and mechanistic aspects for CO_2 reforming of methane over Ni based catalysts, Chem. Eng. J. 278 (2015) 62–78.

[2] S.A. Theofanidis, V.V. Galvita, M. Sabbe, H. Poelman, C. Detavernier, G.B. Marin, Controlling the stability of a Fe–Ni reforming catalyst: Structural organization of the active components, Appl. Catal. B: Environ. 209 (2017) 405–416.

[3] C. Liu, J. Ye, J. Jiang, Y. Pan, Progresses in the preparation of coke resistant Ni-based catalyst for steam and CO_2 reforming of methane, ChemCatChem 3 (2011) 529–541.

[4] X. Li, D. Li, H. Tian, L. Zeng, Z.-J. Zhao, J. Gong, Dry reforming of methane over Ni/La_2O_3 nanorod catalysts with stabilized Ni nanoparticles, Appl. Catal. B: Environ. 202 (2017) 683–694.

[5] J. Niu, X. Du, J. Ran, R. Wang, Dry (CO_2) reforming of methane over Pt catalysts studied by DFT and kinetic modeling, Appl. Surf. Sci. 376 (2016) 79–90.

[6] Petar Djinović, Albin Pintar, Stable and selective syngas production from dry CH_4-CO_2 streams over supported bimetallic transition metal catalysts, Appl. Catal. B: Environ. 206 (2017) 675–682.

[7] E.L. Gubanova, Y. Schuurman, V.A. Sadykov, C. Mirodatos, A.C. van Veen, Evaluation of kinetic models for the partial oxidation of methane to synthesis gas over a Pt/PrCeZrOx catalyst coated on a triangular monolith, Chem. Eng. J. 154 (2009) 174–184.

[8] S. Kawi, Y. Kathiraser, J. Ni, U. Oemar, Z. Li, E.T. Saw, Progress in synthesis of highly active and stable nickel-based catalysts for carbon dioxide reforming of methane, ChemSusChem 8

(2015) 3556–3575.

[9] C. Fan, Y.A Zhu, M.L. Yang, Z.J. Sui, X.G. Zhou, D. Chen, Density functional theory-assisted microkinetic analysis of methane dry reforming on Ni catalyst, Ind. Eng. Chem. Res. 54 (2015) 5901−5913.

[10]T. Kodama, A. Kiyama, K.I. Shimizu, Catalytically activated metal foam absorber for light-to-chemical energy conversion via solar reforming of methane, Energy Fuels 17 (2003) 13–17.

[11]D. Pakhare, J. Spivey, A review of dry (CO_2) reforming of methane over noble metal catalysts, Chem. Soc. Rev. 43 (2014) 7813−7837.

[12]Z. Wang, X.M. Cao, J. Zhu, P. Hu, Activity and coke formation of nickel and nickel carbide in dry reforming: A deactivation scheme from density functional theory, J. Catal. 311 (2014) 469–480.

[13]Z. Shang, S. Li, L. Li, G. Liu, X. Liang, Highly active and stable alumina supported nickel nanoparticle catalysts for dry reforming of methane, Appl. Catal. B: Environ. 201 (2017) 302–309.

[14]J. Ni, L. Chen, J. Lin, S. Kawi, Carbon deposition on borated alumina supported nano-sized Ni catalysts for dry reforming of CH_4, Nano Energy 1 (2012) 674–686.

[15]I.G. Osojnik Crnivec, P. Djinovic, B. Erjavec, A. Pintar, Effect of synthesis parameters on morphology and activity of bimetallic catalysts in CO_2–CH_4 reforming, Chem. Eng. J. 207–208 (2012) 299–307.

[16]T.D. Gould, A. Izar, A.W. Weimer, J.L. Falconer, J.W. Medlin, Stabilizing Ni catalysts by

molecular layer deposition for harsh, dry reforming conditions, ACS Catal. 4 (2014) 2714–2717.

[17]J.W. Han, C. Kim, J.S. Park, H. Lee, Highly coke-resistant Ni nanoparticle catalysts with minimal sintering in dry reforming of methane, ChemSusChem 7 (2014) 451–456.

[18]J.W. Han, J.S. Park, M.S. Choi, H. Lee, Uncoupling the size and support effects of Ni catalysts for dry reforming of methane, Appl. Catal. B: Environ. 203 (2017) 625–632.

[19]S. Gaur, D.J. Haynes, J.J. Spivey, Rh, Ni, and Ca substituted pyrochlore catalysts for dry reforming of methane, Appl. Catal. A: Gen. 403 (2011) 142–151.

[20]T.D. Gould, M.M. Montemore, A.M. Lubers, L.D. Ellis, A.W. Weimer, J.L. Falconer, J.W. Medlin, Enhanced dry reforming of methane on Ni and Ni-Pt catalysts synthesized by atomic layer deposition, Appl. Catal. A: Gen. 492 (2015) 107–116.

[21]S. De, J. Zhang, R. Luque, N. Yan, Ni-based bimetallic heterogeneous catalysts for energy and environmental applications, Energy Environ. Sci. 9 (2016) 3314–3347.

[22]J.H. Bitter, K. Seshan, J.A. Lercher, Mono and bifunctional pathways of CO_2/CH_4 reforming over Pt and Rh based catalysts, J. Catal. 176 (1998) 93–101.

[23]J. Guo, H. Lou, L. Mo, X. Zheng, The reactivity of surface active carbonaceous species with CO_2 and its role on hydrocarbon conversion reactions, J. Mol. Catal. A: Chem. 316 (2010) 1–7.

[24]A.N.J. van Keulen, K. Seshan, J. Hoebink, J.R.H. Ross, TAP investigations of the CO_2 reforming of CH_4 over Pt/ZrO_2, J. Catal. 166 (1997) 306–314.

[25]K.Y. Koo, H.S. Roh, U.H. Jung, W.L. Yoon, CeO_2 promoted Ni/Al_2O_3 catalyst in combined steam and carbon dioxide reforming of methane for gas to liquid (GTL) process, Catal. Lett. 130

(2009) 217–221.

[26]R.Q. Yang, C.A. Xing, C.X. Lv, L. Shi, N. Tsubaki, Promotional effect of La_2O_3 and CeO_2 on Ni/γ-Al_2O_3 catalysts for CO_2 reforming of CH_4, Appl. Catal. A 385 (2010) 92–100.

[27]S. Corthals, J.V. Nederkassel, J. Geboers, H.D. Winne, J.V. Noyen, B. Moens, B. Sels, P. Jacobs, Influence of composition of $MgAl_2O_4$ supported $NiCeO_2ZrO_2$ catalysts on coke formation and catalyst stability for dry reforming of methane, Catal. Today 138 (2008) 28–32.

[28]J.A.C. Dias, J.M. Assaf, Influence of calcium content in Ni/CaO/γ-Al_2O_3 catalysts for CO_2-reforming of methane, Catal. Today 85 (2003) 59–68.

[29]H. Liu, D. Wierzbicki, R. Debek, M. Motak, T. Grzybek, P.D. Costa, M.E. Gálvez, La-promoted Ni-hydrotalcite-derived catalysts for dry reforming of methane at low temperatures, Fuel 182 (2016) 8–16.

[30]C.E. Daza, S. Moreno, R. Molina, Ce-incorporation in mixed oxides obtained by the self-combustion method for the preparation of high performance catalysts for the CO_2 reforming of methane, Catal. Commun.12 (2010) 173–179.

[31]C.E. Daza, C.R. Cabrera, S. Moreno, R. Molina, Syngas production from CO_2 reforming of methane using Ce-doped Ni-catalysts obtained from hydrotalcites by reconstruction method, Appl. Catal. A: Gen. 378 (2010) 125–133.

[32]R. Dębek, M. Motak, D. Duraczyska, F. Launay, M.E. Galvez, T. Grzybek, P.D. Costa, Methane dry reforming over hydrotalcite-derived Ni–Mg–Al mixed oxides: the influence of Ni content on catalytic activity, selectivity and stability, Catal. Sci. Technol. 6 (2016) 6705–6715.

[33]H. Wang, D.W. Blaylock, A.H. Dam, S.E. Liland, K.R. Rout, Y.A. Zhu, W.H. Green, A. Holmen, D. Chen, Steam methane reforming on a Ni-based bimetallic catalyst: density functional theory and experimental studies of the catalytic consequence of surface alloying of Ni with Ag, Catal. Sci. Technol. 7 (2017) 1713–1725.

[34]E. Ochoa-Fernández, C. Lacalle-Vilà, K.O. Christensen, J.C. Walmsley, M. Rønning, A. Holmen, D. Chen, Ni catalysts for sorption enhanced steam methane reforming, Top. Catal. 45 (2007) 3–8.

[35]L. He, H. Berntsen, E. Ochoa-Fernandez, J.C. Walmsley, E.A. Blekkan, D. Chen, Co-Ni catalysts derived from hydrotalcite-like materials for hydrogen production by ethanol steam reforming, Top. Catal. 52 (2009) 206–217.

[36]R. Dębek, M. Radlik, M. Motak, M.E. Galvez, W. Turek, P. Da Costa, T. Grzybek, Ni-containing Ce-promoted hydrotalcite derived materials as catalysts for methane reforming with carbon dioxide at low temperature – on the effect of basicity, Catal. Today 257 (2015) 59–65.

[37]N. Laosiripojana, S. Assabumrungrat, Methane steam reforming over Ni/Ce–ZrO_2 catalyst: Influences of Ce–ZrO_2 support on reactivity, resistance toward carbon formation, and intrinsic reaction kinetics, Appl. Catal. A: Gen. 290 (2005) 200–211.

[38]R. Dębek, M.E. Galvez, F. Launay, M. Motak, T. Grzybek, P. Da Costa, Low temperature dry methane reforming over Ce, Zr and CeZr promoted Ni–Mg–Al hydrotalcite-derived catalysts, Int. J. Hydrogen Energy 21 (2016) 11616–11623.

[39]R. Dębek, M. Motak, M.E. Galvez, T. Grzybek, P. Da Costa, Promotion effect of zirconia on

Mg(Ni,Al)O mixed oxides derived from hydrotalcites in CO_2 methane reforming, Appl. Catal. B: Environ. 223 (2018) 36–46.

[40]B. Koubaissy, A. Pietraszek, A.C. Roger, A. Kiennemann, CO_2 reforming of methane over Ce–Zr–Ni–Me mixed oxides, Catal. Today 157 (2010) 436–439.

[41]M. Sharifi, M. Haghighi, F. Rahmani, S. Karimipour, Syngas production via dry reforming of CH_4 over Co- and Cu- promoted Ni/Al_2O_3-ZrO_2 nanocrystals synthesized via sequential impregnation and sol–gel methods, J. Natural Gas Sci. Eng. 21 (2014) 993–1004.

[42]M.C. Payne, M.P. Teter, D.C. Allan, T.A. Arias, J.D. Joannopoulos, Iterative minimization techniques for ab initio total-energy calculations: molecular dynamics and conjugate gradients, Rev. Mod. Phys. 64 (1992) 1045–1097.

[43]B. Delley, Fast calculation of electrostatics in crystals and large molecules, J. Phys. Chem. 100 (1996) 6107–6110.

[44]J. Wellendorff, K.T. Lundgaard, A. Mogelhoj, V. Petzold, D.D. Landis, J.K. Norskov, T. Bligaard, K.W. Jacobsen, Density functionals for surface science: Exchange-correlation model development with Bayesian error estimation, Phys. Rev. B 85 (2012) 235149.

[45]F. Studt, F. Abild-Pedersen, J. Varley, J. Nørskov, CO and CO_2 hydrogenation to methanol calculated using the BEEF-vdW functional, Catal. Lett. 143 (2013) 71–73.

[46]H.J. Monkhorst, J.D. Pack, Special points for Brillouin-zone integrations, Phys. Rev. B 13 (1976) 5188–5192.

[47]G. Henkelman, H. Jonsson, A dimer method for finding saddle points on high dimensional

potential surfaces using only first derivatives, J. Chem. Phys. 111 (1999) 7010–7022.

[48]S. Watanabe, X. Ma, C. Song, Characterization of structural and surface properties of nanocrystalline TiO_2-CeO_2 mixed oxides by XRD, XPS, TPR, and TPD, J. Phys. Chem. C 113 (2009) 14249–14257.

[49]H.S. Roh, H.S. Potdar, K.W. Jun, Carbon dioxide reforming of methane over co-precipitated Ni–CeO_2, Ni–ZrO_2 and Ni–Ce–ZrO_2 catalysts, Catal. Today 93–95 (2004) 39–44.

[50]R.D. Purohit, S. Saha, A.K. Tyagi, Combustion synthesis of nanocrystalline ZrO_2 powder: XRD, Raman spectroscopy and TEM studies, Mater. Sci. Eng. B 130 (2006) 57–60.

[51]C. Pacholski, A. Kornowski, H. Weller, Self-assembly of ZnO: From nanodots to nanorods, Angew. Chem. Int. Ed. 41 (2002) 1188–1191.

[52]E. Akbari, S. Mehdi Alavi, M. Rezaei, Synthesis gas production over highly active and stable nanostructured Ni-MgO-Al_2O_3 catalysts in dry reforming of methane: Effects of Ni contents, Fuel 194 (2017) 171–179.

[53]G. Leofanti, M. Padovan, G. Tozzola, B. Venturelli, Surface area and pore texture of catalysts, Catal. Today 41 (1998) 207–219.

[54]R.K. Singha, A. Shukla, A. Sandupatla, G. Deo, R. Bal, Synthesis and catalytic activity of a Pd doped Ni–MgO catalyst for dry reforming of methane, J. Mater. Chem. A 5 (2017) 15688–15699.

[55]M. García-Diéguez, I.S. Pieta, M.C. Herrera, M.A. Larrubia, L.J. Alemany, Nanostructured Pt- and Ni-based catalysts for CO_2-reforming of methane, J. Catal. 270 (2010) 136–145.

[56]M. García-Diéguez, I.S. Pieta, M.C. Herrera, M.A. Larrubia, L.J. Alemany, Improved Pt-Ni nanocatalysts for dry reforming of methane, Appl. Catal. A: Gen. 377 (2010) 191–199.

[57]J.M. Wei, E. Iglesia, Isotopic and kinetic assessment of the mechanism of reactions of CH_4 with CO_2 or H_2O to form synthesis gas and carbon on nickel catalysts, J. Catal. 224 (2004) 370–383.

[58]S. Özkara-Aydınoglu, A.E. Aksoylu, A comparative study on the kinetics of carbon dioxide reforming of methane over Pt–Ni/Al_2O_3 catalyst: Effect of Pt/Ni Ratio, Chem. Eng. J. 215–216 (2013) 542–549.

[59]M.F. Mark, W.F. Maier, CO_2-reforming of methane on supported Rh and Ir catalysts J. Catal. 164 (1996) 122–130.

[60]D. Martin, D. Duprez, Mobility of surface species on oxides. 1. Isotopic exchange of $^{18}O_2$ with ^{16}O of SiO_2, Al_2O_3, ZrO_2, MgO, CeO_2, and CeO_2-Al_2O_3. Activation by noble metals. Correlation with oxide basicity, J. Phys. Chem. 100 (1996) 9429–9438.

[61]M. Watanabe, M. Osada, H. Inomata, K. Arai, A. Kruse, Acidity and basicity of metal oxide catalysts for formaldehyde reaction in supercritical water at 673 K, Appl. Catal. A: Gen. 245 (2003) 333–341.

[62]D. Gao, Y. Feng, H. Yin, A. Wang, T. Jiang, Coupling reaction between ethanol dehydrogenation and maleic anhydride hydrogenation catalyzed by Cu/Al_2O_3, Cu/ZrO_2, and Cu/ZnO catalysts, Chem. Eng. J. 233 (2013) 349–359.

[63]J.C. Lavalley, Infrared spectrometric studies of the surface basicity of metal oxides and zeolites using adsorbed probe molecules, Catal. Today 27 (1996) 377–401.

[64]E.V. Anslyn, D.A. Dougherty, Modern Physical Organic Chemistry, University Science Books, 2006.